ELSEVIER

Determination of nonlinear properties of thermal sprayed ceramic coatings via inverse analysis

Toshio Nakamura *, Yajie Liu

Department of Mechanical Engineering, State University of New York at Stony Brook, New York, NY 11794, USA

Abstract

A robust procedure to estimate nonlinear mechanical properties of thermally sprayed (TS) ceramic coatings is introduced. Such a method is valuable particularly for TS coatings since each may possess unique properties depending upon its processing condition. Traditionally, their responses have been assumed as linear elastic (isotropic or anisotropic) except in very high temperature environments where softening may occur. However, recent inspections revealed their properties to be more accurately characterized as nonlinear elastic. It appears their distinctive morphology consisting of cracks and interfaces are responsible for such a response. In this work, a versatile procedure to identify nonlinear properties of thermally sprayed coatings is developed. First, a suitable stress–strain model is proposed and then a nonlinear bi-material beam solution is derived. Afterward, an inverse analysis technique is utilized to process the measured curvature–temperature to extract the unknown parameters. Prior to implementing in actual specimens, a detailed simulation study is performed to verify the method's accuracy as well as robustness. This computational analysis closely replicates deposition processes of TS coatings. With the successful verification, actual curvature measurement of TS yttria-stabilized zirconia (YSZ) coating is used to determine the nonlinear properties. The estimated results clearly reveal a significant nonlinearity of the TS coating. The main advantage of this procedure is that it requires essentially no specimen preparation and allows continuous measurements after TS deposition. Furthermore, the data interpretation does not require complex computational models and calculations. This streamlined process makes the present method attractive when evaluations of many specimens are required. The present procedure can be also extended to identify nonlinear properties of other coatings/films on substrates.
© 2006 Elsevier Ltd. All rights reserved.

Keywords: Thermally sprayed coating; Substrate–curvature measurement; Nonlinear bi-material beam; Inverse analysis; Kalman filter

* Corresponding author. Tel.: +1 631 632 8312; fax: +1 631 632 8544.
  E-mail address: toshio.nakamura@sunysb.edu (T. Nakamura).

1. Introduction

Thermally sprayed (TS) ceramic coatings are employed in many industrial applications, such as aerospace, transportation, petrochemical, electronics and medical. The coatings provide surface protections/insulations against high temperature, wear, corrosion, oxidation, and electrical conduction. As the engineering application increases, their mechanical reliability becomes more critical to ensure designed performances. The coating's properties, such as effective modulus, thermal conductivity and residual stresses, are key factors in understanding coating's reliability (Kesler et al., 1998). Often TS ceramic coatings are synthesized with plasma spray guns where feedstock particles are melted at extreme temperatures. The molten or semi-molten splats solidify rapidly on substrate surfaces to form a coating. This process generates lamellar microstructure as well as many defects such as pores and cracks. Additional micro-cracks also form during cool down when large thermal stresses are generated due to the mismatch of thermal expansion with the substrate. These geometrical attributes make the TS coating's stiffness to be much lower than that of bulk material.

In situ substrate–curvature measurement is an effective technique to determine coating's effective elastic modulus and residual stress. This technique was introduced on the premises that both coating and substrate deform *linearly*, which enables the use of well-known bi-material curvature–temperature formula to identify the elastic modulus as well as the residual stress of coating. Many thermally sprayed materials such as molybdenum indeed exhibit linear responses that justify the applicability of technique (Matejicek et al., 2003). However, recent studies revealed that curvature–temperature measurements of some ceramics do not exhibit linear behavior. These include yittria-stabilized zirconia (YSZ) and alumina (Al_2O_3) that are frequently chosen for thermal barrier applications. At first, the nonlinearity was thought to be the result of partial debonding between coating and substrate or a measurement error during thermal cycle. However after careful inspections, it was confirmed that the coatings themselves indeed display nonlinear responses. In general, its modulus decreases with increasing tensile stress. Note that the maximum temperatures are kept less than 250 °C, which is well below the temperatures when property changes are expected to occur in ceramics.

The nonlinearity appears to arise from unique microstructural attributes of thermally sprayed ceramic coatings. As many micro-cracks and weak interfaces are embedded in the coatings, their opening/closing and sliding generate the nonlinear responses. Under high compressive load, crack faces are closed and the coatings exhibit higher apparent stiffness while opened cracks under tensile state produce more compliant response (Kroupa and Dubsky, 1999; Kroupa and Plesek, 2002). Since micro-cracks have various orientations/sizes, closings and openings do not occur simultaneously. Such random features result in a smooth variation of effective modulus rather than a sudden change expected from a single crack model. At room temperature, high residual compressive stress keeps many cracks to be closed. The nonlinear behaviors of ceramic coatings were also observed under other tests. Harok and Neufuss (2001) reported such behavior of atmospheric plasma sprayed (APS) ZrSiO4 under four-point bend tests. Waki et al. (2004) observed the nonlinear stress–strain responses of plasma sprayed zirconia coating using the laser speckle strain–displacement gauge (SSDG). Wang et al. (2006) showed nonlinear stress–strain relation of thermally sprayed metallic Ni–45Cr coating under tensile loading along the through-thickness direction due to its lamellar features.

In this paper, a novel procedure based on a nonlinear beam model and an inverse analysis is proposed to estimate the nonlinear stress–strain relations of TS ceramics coatings. Essentially, this method extracts the best estimates of unknown material parameters from measured curvature–temperature data during thermal cycle tests.

2. Substrate–curvature measurements

2.1. Background

A thermal cycle test to measure curvature change is an effective method to estimate an unknown modulus of coating or thin film. The curvature measurement to determine properties of *thin* films on thick substrate was introduced by Stoney (1909). The substrate–curvature method based on Stoney formula has been widely used in various applications (e.g., Carlotti et al., 1997; Lacquaniti et al., 1997; Krulevitch et al., 1996; Hunsche et al., 2001; Oka et al., 2003; Menzel et al., 2005). Kuroda et al. (1988, 1990) have also utilized the formula

for TS coatings. The simple form of Stoney formula makes determinations of material properties straightforward. Obviously the limitation of this formula is that the thickness of film or coating must be sufficiently small as compared to that of substrate. For films and coatings that are thick, curvature solutions must be obtained with an alternate method. If the total thickness (film plus substrate) is still small compared to the specimen length, one can still invoke the beam/plate theory to establish the curvature formula.

Although there are other means to measure the modulus of coating bonded to a substrate, the curvature measurement under temperature change offers several advantages. First, an inaccuracy associated with measurement error is less than that from tensile tests. For an example, if the modulus ratio of coating over substrate is ~0.40 (close to many TS YSZ-Al system) and the thickness of coating is 20% of that of substrate, 1% error in the displacement measurement under *uniaxial tensile test* magnifies the error in modulus estimation by 14%. With the curvature test, it would be 6% error. Second, the thermal loading produces more *uniform* stress state within the coating than that under mechanical load. For an example, with three-point-bend test, local stress concentrations and associated measurement errors at the loading points are inevitable. Obviously near-uniform stress and deformation states are more ideal for property measurements.

Within thermally sprayed coatings, the state of stress evolves as follows (Matejicek and Sampath, 2003; Tsui and Clyne, 1997). During deposition to fabricate the coating, molten particles strike onto a substrate or previous splats (solidified particles) and immediately cool down. As their temperatures rapidly drop and solidify, high quenching stresses develop. The nonequilibrium thermal conditions produce an overall tensile state within the coating. At the end of deposition, the large tensile stresses in the coating cause a sizable specimen curvature. However as both coating and substrate cool down, their mismatch in coefficients of thermal expansion (CTE) generates additional thermal stresses. Since CTE of ceramic coating is generally less than that of metallic substrates, the cooling tends the coatings to be compressive. For most YSZ-Al systems, due to the large CTE difference, the *overall* or *net* stresses at the room temperature within the coating are usually compressive although stress states vary locally due to high stresses generated during solidifications. The magnitude of residual stress also depends on the pre-heating temperature of substrate, substrate and coating thicknesses and other spray processing parameters (e.g., feedstock, powder sizes, particle temperature and velocity).

If both coating and substrate are assumed to be linear elastic, the curvature change during spraying and cooling can be expressed in terms of effective strain change as (Tsui and Clyne, 1997)

$$\Delta\kappa = \frac{6E_s E_c ht(h+t)\Delta\varepsilon}{E_s^2 h^4 + E_c^2 t^4 + 2E_s E_c ht(2h^2 + 3ht + 2t^2)} \tag{1}$$

Here, E_s and E_c are the moduli, h and t are the thicknesses of substrate and coating, respectively. The strain change during spraying is $\Delta\varepsilon = \alpha_c\Delta T$ and for cooling it is $\Delta\varepsilon = (\alpha_s - \alpha_c)\Delta T$, where ΔT is the corresponding temperature change, α_s and α_c are the thermal expansion coefficients of substrate and the coating, respectively. The above equation and measured $\Delta\kappa$–ΔT record can be used to determine the coating modulus E_c (via the quadratic formula). For a nonlinear coating, a different beam theory formulation is necessary as described in Section 3.

2.2. Experimental procedure

In the present experiments, the curvature–temperature records from post-deposition thermal cycle are utilized to determine the nonlinear property. Typical in-plane dimensions of specimens are 230 mm × 25.4 mm. The thickness of coating vary $t = 250$–$800\ \mu m$ while that of substrate is about $h = 3$ mm. At the bottom of substrate, three sensors are attached (70 mm apart) to measure the deflections with Aromat LM-10 laser with 1 μm resolution. During the thermal cycle, the specimen is heated with a gas torch gun moving across YSZ coating surface until the temperature reaches about 250 °C (measured by a thermocouple attached to the substrate bottom). Afterward, the specimen is cooled down to the room temperature under forced air convection. Typically it takes 2 min to heat up and more than 7 min to cool down. Due to uneven heating conditions, the curvature record is generally not stable during the heating phase. Thus for the property identification, the measurements during the cool down period are used. Furthermore, at the end of heating (or the initial phase

of cool down), the temperature within the specimen is still not uniform. Thus the measurements obtained during first few seconds of cooling ($\Delta T \sim 40$ °C) are discounted. Note it takes about 2–3 s to reach the thermal equilibrium across the entire length of specimen. Although not shown here, many specimens indeed exhibited unstable results at this initial cool down phase.

The schematic of specimen curvature changes is illustrated in Fig. 1(a). At the beginning of cool down ($T = 230$–250 °C), the coating is in tension. But as the temperature decreases, the state of stress in the coating changes to compression. The measured curvature–temperature record for APS YSZ coating on aluminum (Al6061) substrate is shown in Fig. 1(b). The thickness of this coating is 434 μm while that of substrate is 3.2 mm. The feedstock is fused and crushed YSZ powder and it was sprayed at average particle temperature of 2550 °C with velocity of 85 m/s. In the figure, the temperature corresponding to zero-curvature is denoted as T_0. It can be also observed that the curve is steeper at lower temperature, which suggests a higher stiffness of coating near the room temperature T_R. As noted earlier, YSZ is not expected to be thermally dependent in this temperature range. Thus the nonlinearity is driven by the geometrical attributes under stress changes. The nonlinear curvature–temperature behavior of YSZ coating was also confirmed in a separate measurements carried out with a surface profilometer Tencor FLX-2900 laser scanning system. Here, both heating and cooling rates were set very low so that the thermal equilibrium was maintained throughout the test.

During the development of present procedure described next, the measurements of many different specimens are referenced and considered. However to avoid making the paper lengthy, and since the main objec-
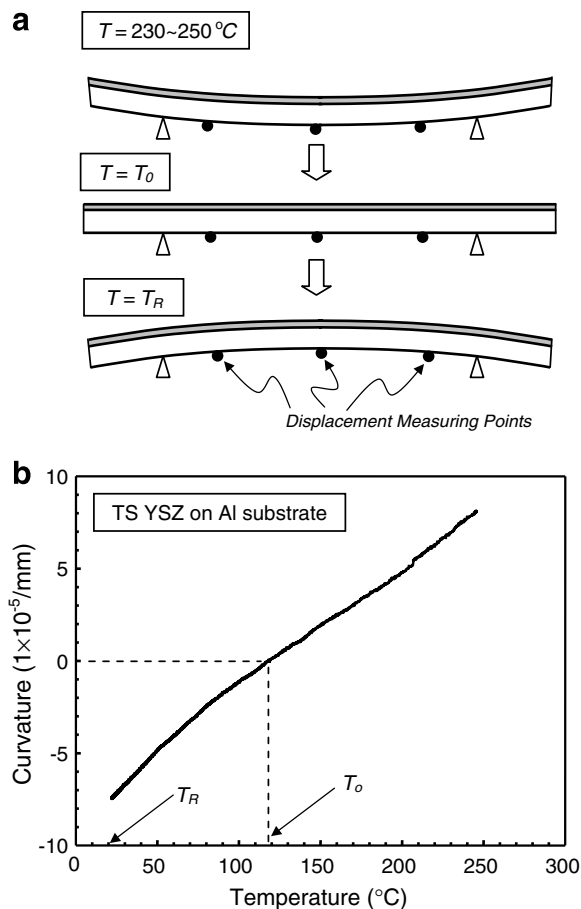

Fig. 1. (a) Schematic of curvature change as coating and substrate is cooled down during thermal cycle test. Here, T_0 denotes the temperature when the curvature is zero and T_R is the room temperature. (b) Experimentally measured curvature–temperature relation of YSZ coating on Al substrate during cool down.

tives are to introduce and verify the present procedure, only one experimental record is included here. Separate papers will report measurements of other TS coatings including the one measured by the laser scanning system.

3. Proposed procedure

3.1. Constitutive model

In order to describe the coating's nonlinear behavior, a phenomenological constitutive model is introduced. First, based on the experimental observations and likely physical causes of nonlinearity (cracks and defects), the stress–strain relation is set to be asymmetric under tension and compression. Second, under very large compression, the response should be nearly linear since many cracks and thin defects are closed. Third, experimental records suggest continuous change of coating stiffness. With these factors and to keep the number of required parameters to minimum, we propose the following uniaxial stress–strain model for TS ceramic coatings:

$$\varepsilon = \begin{cases} \frac{\sigma}{E} & \text{for } \sigma < 0 \\ \frac{\sigma}{E} + \frac{\sigma^n}{E\sigma_0^{n-1}} & \text{for } \sigma \geqslant 0 \end{cases} \tag{2}$$

Essentially, the above equation is a combination of linear elastic model under compression and Ramberg–Osgood model under tension. Here, E is the Young's modulus, n is the power-law exponent and σ_0 is the reference stress (not yield stress). However after careful inspections and comparisons with experimental measurements, it was found that the above model does not describe the coating's effective property accurately. In fact the transitions from linear to nonlinear generally do not occur at the zero stress ($\sigma = 0$). In order to accommodate this response, the following modified model is established:

$$\varepsilon = \begin{cases} \frac{\sigma}{E} + \frac{\sigma_T^n}{E\sigma_0^{n-1}} & \text{for } \sigma < \sigma_T \\ \frac{\sigma}{E} + \frac{(\sigma-\sigma_T)^n + \sigma_T^n}{E\sigma_0^{n-1}} & \text{for } \sigma \geqslant \sigma_T \end{cases} \tag{3}$$

In the above expression, the transitional stress σ_T where the change *from linear to nonlinear* relations occurs is introduced. In most tests conducted for TS YSZ, the transitional stresses are in compression (i.e., $\sigma_T < 0$). The schematic of stress–strain curve according to (3) is shown in Fig. 2. Here, the stress–strain axes (σ^*–ε^*) centered at $\sigma = \sigma_T$ are also illustrated to distinguish the linear and nonlinear regimes. In fact the stress–strain relation with respect to these axes follows (2). The relation (3) turns out to be very versatile to describe the stress–strain behavior of TS coatings with minimum number of parameters (E, σ_0, n and σ_T). Note this model is C^1 contin-
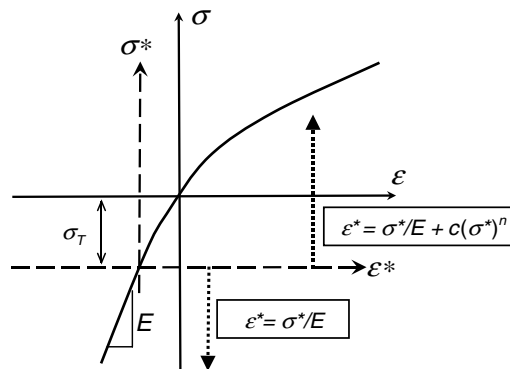

Fig. 2. Nonlinear stress–strain relation model for TS ceramic coatings. Change in linear and nonlinear stress–strain relation occurs at transitional stress σ_T. Corresponding equations are noted below and above the ε^* axis, respectively.

uous at $\sigma = \sigma_T$. Under multi-dimensional condition, the Poisson's ratio v is also required. Also note that E is more appropriately described as the *elastic tangent modulus* near the room temperature since it is not the elastic modulus at $\sigma = 0$. As noted, σ_0 is simply a reference parameter which defines the nonlinear relationship. Once these parameters are determined, the residual stress σ_R at room temperature can be also extracted.

Though not presented here, many measured data are used to examine the suitability of the proposed material model. Other forms of stress–strain relation describing the mechanical behavior of TS coatings are also possible but they would probably require more parameters. Note that a bilinear type relation with three parameters would not be consistent with the measured curvature–temperature data.

3.2. Nonlinear bi-material beam solution

One of the major aims of this study is to develop a robust procedure without requiring large- scale computations such as a finite element analysis. Thus if a closed-form relation between the curvature data and the stress–strain model can be established, the post-processing to identify the unknown parameters can be carried out effectively. Here, the formulation for nonlinear bi-material beam solution is described. It models a nonlinear layer attached to a linear elastic layer. Although this procedure is straightforward, its derivation is rather complex due to shifting of the neutral axis as effective coating stiffness varies. Furthermore, although there have been studies on large deformation effects on beams and plates (e.g., Finot and Suresh, 1996), we were not able to find solutions for the nonlinear elastic bi-material beams.

Suppose a bi-material specimen consists nonlinear elastic coating and linear elastic substrate as shown in Fig. 3. With temperature change, the axial strain in the coating is

$$\varepsilon_c(y) = -\Delta\kappa(y - y_0) + \alpha_c\Delta T + \frac{F_{mis}}{bE_c^*t}. \tag{4}$$

Here, $\Delta\kappa$ is the curvature change under temperature variation ΔT, α_c is the coefficient of thermal expansion, y_0 is the location of neutral axis, F_{mis} is the mismatch force, b is the specimen width, t is the coating thickness and E_c^* is the secant modulus defined as $E_c^* = \sigma_c/\varepsilon_c^m$. Also σ_c is the axial stress and ε_c^m is the mechanical strain (i.e., $\varepsilon_c^m(y) = \varepsilon_c(y) - \varepsilon_c^{therm}$) in the coating. Unlike linear elastic coatings, the neutral axis shifts with change in the secant modulus as

$$y_0 = \frac{E_s h^2/2 + \int_h^{h+t} E_c^*(y)y\,dy}{E_s h + \int_h^{h+t} E_c^*(y)\,dy}. \tag{5}$$

Here, E_s and h are the Young's modulus and thickness of substrate, respectively. So-called mismatch force (per width) in the coating and the substrate may be computed as

$$\frac{F_{mis}}{b} = -\int_h^{h+t} \sigma_c(y)\,dy = \frac{E_s E_{ave}^* ht}{E_s h + E_{ave}^* t}\Delta\alpha\Delta T. \tag{6}$$

In the above, $\Delta\alpha = \alpha_s - \alpha_c$ and E_{ave}^* is introduced as the average secant modulus within the coating. Similarly, the moment generated by the mismatch force can be shown as

$$\frac{M_{mis}}{b} = \frac{F_{mis}}{b}\left(\frac{h+t}{2}\right) = \frac{E_s E_{ave}^* ht}{E_s h + E_{ave}^* t}\left(\frac{h+t}{2}\right)\Delta\alpha\Delta T. \tag{7}$$
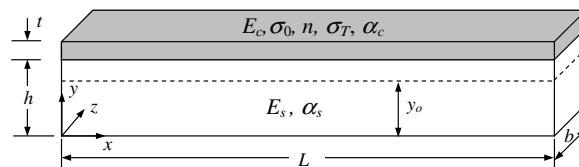

Fig. 3. Schematic of TS coating on substrate with relevant dimensions. Corresponding material parameters are noted and the location of neutral axis y_0 is shown.

The curvature change relates to the moment as $\Delta\kappa = M_{\mathrm{mis}}/(EI)_{\mathrm{bi}}$. Here, $(EI)_{\mathrm{bi}}$ is the moment of inertia of bi-material beam which is not constant. It can be computed as

$$\frac{(EI)_{\mathrm{bi}}}{b} = E_s h\left(\frac{h^2}{3} - hy_0 + y_0^2\right) + \int_h^{h+t} E_c^*(y)(y - y_0)^2\, \mathrm{d}y \tag{8}$$

With these relations, the curvature change may be expressed as

$$\Delta\kappa = \frac{\frac{E_s E_{\mathrm{ave}}^* ht}{E_s h + E_{\mathrm{ave}}^* t}\left(\frac{h+t}{2}\right)\Delta\alpha\Delta T}{E_s h\left(\frac{h^2}{3} - hy_0 + y_0^2\right) + \int_h^{h+t} E_c^*(y)(y - y_0)^2\, \mathrm{d}y}. \tag{9}$$

Since the neutral axis shifts with the temperature, the above formula requires several implicit (iterative) operations for a given ΔT. The iteration loops can be reduced by assuming the following form:

$$\Delta\kappa \cong \frac{6 E_s E_{\mathrm{ave}}^* ht(h + t)\Delta\alpha\Delta T}{E_s^2 h^4 + E_{\mathrm{ave}}^{*2} t^4 + 2 E_s E_{\mathrm{ave}}^* ht(2h^2 + 3ht + 2t^2)}. \tag{10}$$

In the above, the secant modulus $E_c^*(y)$ in the integral (9) is replaced with the average value E_{ave}^* through the coating thickness. A similar assumption can be taken for the computation of y_0 in (5). To further reduce the computational requirement, instead of computing the correct average value, E_{ave}^* can be estimated at the mid-point of coating ($y = h + t/2$) as

$$E_{\mathrm{ave}}^* \cong \frac{\sigma(\varepsilon_c^{\mathrm{mid}})}{\varepsilon_c^{\mathrm{mid}}}, \quad \text{where } \varepsilon_c^{\mathrm{mid}} = -\Delta\kappa\left(h + \frac{t}{2} - y_0\right) + \frac{E_s h}{E_s h + E_{\mathrm{ave}}^* t}\Delta\alpha\Delta T \tag{11}$$

Obviously, the computation of E_{ave}^* still requires multiple iterations. The curvature formula (10) for the *non-linear* beam appears to be similar to the one given for the *linear elastic* bi-material beam (1). However, the required computations are *very different* and the determination of unknown material properties for a given $\Delta\kappa$–ΔT record is not a simple process.

The expression (10) suggests an incremental process to determine $\Delta\kappa$ for a given temperature change ΔT. First, the axial strain at mid-point is initialized with an approximation as $\varepsilon = \Delta\alpha\Delta T$ (note $\varepsilon = \varepsilon_c^{\mathrm{mid}}$). Then the stress is computed via the constitutive equation (3) with iterations. Once the average secant modulus and neutral axis are calculated via (11) and (5), the curvature can be solved. With this curvature, the strain is updated and the convergence is checked. The iteration is repeated until the required tolerance, generally set as $\Delta\alpha\Delta T/100$, is met. This process is illustrated in Fig. 4. The calculations of stresses and secant modulus are described in the appendix.

3.3. Procedure to determine unknown parameters

According to the proposed constitutive equation, the unknown parameters are E_c, σ_0, n and σ_T. We propose a multi-step procedure to estimate these parameters. First, the tangent modulus E_c near the room temperature is computed prior to the other parameters associated with the nonlinear behavior. In order to determine this modulus, the linear portion of curvature–temperature is identified as shown in Fig. 5. Using the slope of curve ($\Delta\kappa/\Delta T$) and the bi-material formula for linear elastic materials (1), one can solve for E_c with the quadratic formula.

Next the determination of the nonlinear parameters is carried out. Here, the process can be simplified by shifting T and κ coordinates as $T^* = T - T_T$ and $\kappa^* = \kappa - \kappa_T$, respectively. These shifts enable computations of σ_0 and n according to (2) instead of more complex expression (3). The stress and strain are re-adjusted once the parameters determined. To obtain the best estimates of σ_0 and n from the curvature–temperature ($T > T_T$), we utilize Kalman filter algorithm as described in the next section. Then the transitional stress σ_T is computed at $T = T_T$ and also the residual stress σ_R at room temperature (20 °C) is determined. The detailed derivations of these stresses are described in the appendix.

$$\boxed{\begin{array}{c}\text{Initialize}\\ \varepsilon_0 = \Delta\alpha\Delta T \ \text{and} \ i = 0\end{array}}$$

$$\boxed{\text{Set} \ i = i + 1}$$

$$\boxed{\begin{array}{c}\text{Compute stress} \ \sigma(\varepsilon_i)\\ \text{Update average secant modulus}\\ (E_{ave}^*)_i = \sigma(\varepsilon_i)/\varepsilon_i\\ \text{Compute neutral axis}\\ y_o = \dfrac{E_s h^2 + (E_{ave}^*)_i^2 t^2 + 2(E_{ave}^*)_i ht}{2\left[E_s h + (E_{ave}^*)_i t\right]}\\ \text{Update curvature}\\ (\Delta\kappa)_i = \dfrac{6E_s(E_{ave}^*)_i h\,t(h+t)\Delta\alpha\Delta T}{E_s^2 h^4 + (E_{ave}^*)_i^2 t^4 + 2E_s(E_{ave}^*)_i h\,t(2h^2 + 3ht + 2t^2)}\end{array}}$$

$$\boxed{\begin{array}{c}\text{Update strain}\\ \varepsilon_i = -(\Delta\kappa)_i\left(h + \dfrac{t}{2} - y_o\right) + \dfrac{E_s h}{E_s h + (E_{ave}^*)_i t}\Delta\alpha\Delta T\end{array}}$$

$$\left\langle\begin{array}{c}\text{Check convergence}\\ |\varepsilon_i - \varepsilon_{i-1}| < \text{TOL}\end{array}\right\rangle \quad \text{No}$$

Yes

$$\boxed{\begin{array}{c}\text{Set}\\ \Delta\kappa = (\Delta\kappa)_i\end{array}}$$
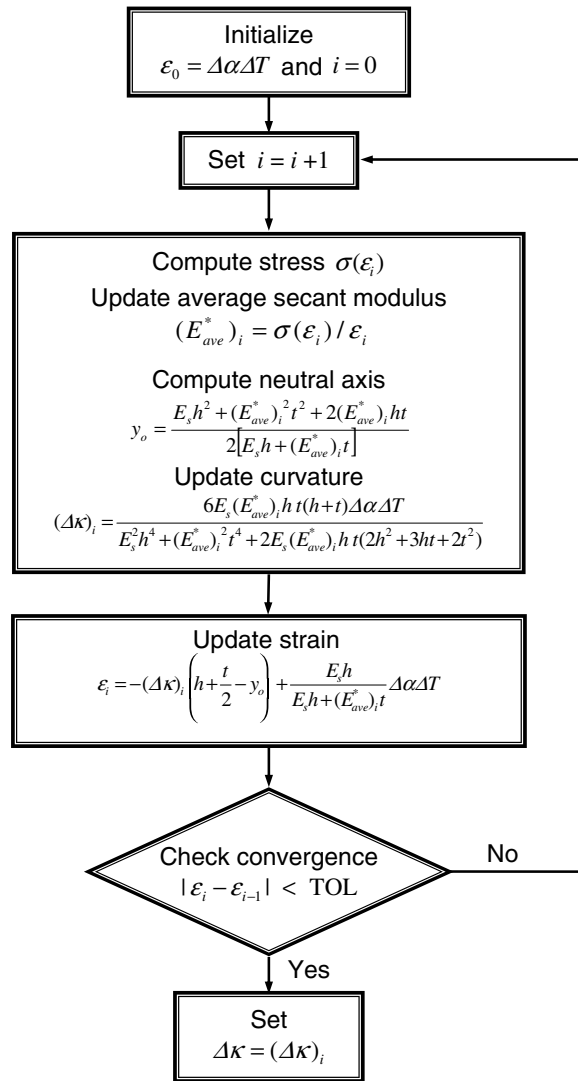
Fig. 4. Flowchart to compute curvature $\Delta\kappa$ for a given temperature change ΔT.
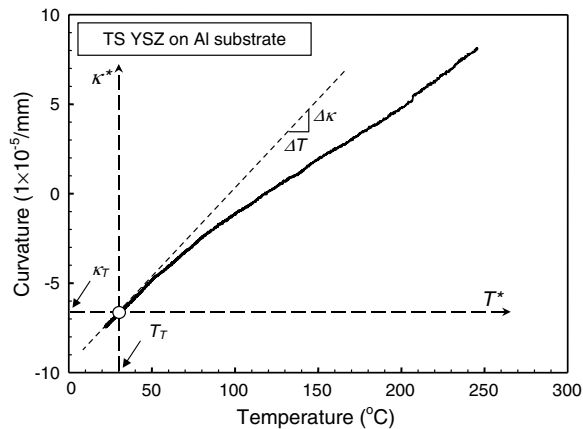

Fig. 5. Identification of transitional point (linear to nonlinear) to extract initial tangent modulus E_c from ΔT and $\Delta\kappa$. Shifted coordinates centered at T_T and κ_T are also shown.

4. Inverse analysis

An inverse analysis is a method by which unknown state parameters are estimated from indirect measurements. Here, the present inverse analysis utilizes Kalman filter technique (Kalman, 1960) to estimate the unknown material properties, namely, the reference stress σ_0 and the power-law exponent n. The Kalman filter algorithm has an advantage over other adaptive algorithms through its fast convergence to optimal solutions in nonlinear problems. It is also suited for this type problem where substantial noise is contained in the measurements. Basically, the Kalman Filter algorithm updates the previous estimates based on indirect measurements of unknown state variables and covariance information and attempts to find the best estimate. It has been utilized in other mechanical problems (e.g., Gu et al., 2003; Vaddadi et al., 2003). In the formulation, two unknown parameters are represented in a state vector form as $\boldsymbol{x}_t = [(\sigma_0)_t, (n)_t]^\mathrm{T}$. Here, t may represent the actual time as well as the temperature (e.g., from $T_{\min}$ to $T_{\max}$). The procedure is carried out with the following updating equation:

$$\boldsymbol{x}_t = \boldsymbol{x}_{t-1} + \boldsymbol{K}_t[\kappa_t^{\mathrm{meas}} - \kappa_t(\boldsymbol{x}_{t-1})] \tag{12}$$

Here, $\boldsymbol{K}_t$ is the 'Kalman gain matrix' and κ_t^{meas} is the measured curvature at t. Also $\kappa_t(\boldsymbol{x}_{t-1})$ is a curvature computed with estimated state parameters at the previous increment. Note that these computations require solutions of curvature for a given set of state parameters. Such solutions are sometimes referred as the forward solutions. In the above equation, the Kalman gain matrix multiplies the difference between the measured and computed curvature to make corrections to the unknown state parameters. The Kalman gain matrix is computed as

$$\boldsymbol{K}_t = \boldsymbol{P}_t(\boldsymbol{\kappa}_t')^\mathrm{T} \boldsymbol{R}_t^{-1}, \quad \text{where} \quad \boldsymbol{P}_t = \boldsymbol{P}_{t-1} - \boldsymbol{P}_{t-1}(\boldsymbol{\kappa}_t')^\mathrm{T}(\boldsymbol{\kappa}_t'\boldsymbol{P}_{t-1}\boldsymbol{\kappa}_t'^{T} + \boldsymbol{R}_t)^{-1}\boldsymbol{\kappa}_t'\boldsymbol{P}_{t-1} \tag{13}$$

With two state and one measured parameters, the size of Kalman gain matrix is 2×1. Also $\boldsymbol{\kappa}_t'$ is a vector that contains the gradients of κ_t with respect to the state parameters as

$$\boldsymbol{\kappa}_t' = \frac{\partial \kappa_t}{\partial x_t} = \begin{pmatrix} \frac{\partial \kappa_t}{\partial \sigma_0} \\ \frac{\partial \kappa_t}{\partial n} \end{pmatrix} \tag{14}$$

In addition, $\boldsymbol{P}_t$ is the 'measurement covariance matrix', related to the range of unknown state parameters at increment t, and $\boldsymbol{R}_t$ is the 'error covariance matrix', related to the size of measurement error. Once the initial values are imposed, $\boldsymbol{P}_t$ is updated every step while $\boldsymbol{R}_t$ is prescribed at each step. In many cases, fixed values can be assigned to the components of $\boldsymbol{R}_t$ as long as measurement error bounds do not vary substantially during the measurements. Since the convergence rate is sensitive to the values of $\boldsymbol{P}_t$ and $\boldsymbol{R}_t$, proper assignments for these two matrices are essential. The initial measurement covariance matrix $\boldsymbol{P}_0$ and the error covariance matrix $\boldsymbol{R}_t$ are set as

$$\boldsymbol{P}_0 = \begin{pmatrix} (\Delta\sigma_0)^2 & 0 \\ 0 & (\Delta n)^2 \end{pmatrix} \quad \text{and} \quad \boldsymbol{R}_t = ((\kappa^{\mathrm{err}})^2). \tag{15}$$

Here, $\Delta\sigma_0$ and Δn denote the predicted ranges of the unknown parameters (i.e., domain of unknowns), respectively. While $\boldsymbol{P}_0$ is diagonal, (13) results in a filled $\boldsymbol{P}_t$ matrix during subsequent increments. In the current analysis, the component of $\boldsymbol{R}_t$ is chosen based on the estimated measurement error for the curvature measurements. The values of κ^{err} was set approximately 4% of the largest curvature. The Kalman filter procedure, which is summarized in Fig. 6, was implemented in a computational code.

In many inverse analyses, forward solutions are constructed through finite element computations for some combinations of state parameters. Then the reference data or the measurement parameters and their gradients can be computed via interpolation functions. However in this problem, the closed-form curvature–temperature is established (albeit with numerical iterations), and the required parameters κ_t in (12) and $\boldsymbol{\kappa}_t'$ in (13) can be obtained without complex computational analyses. This feature is particularly attractive since a single code can be developed to estimate the material property of nonlinear TS coating without performing separate calculations. The expressions for these parameters with the proposed constitutive equation are shown in the appendix.
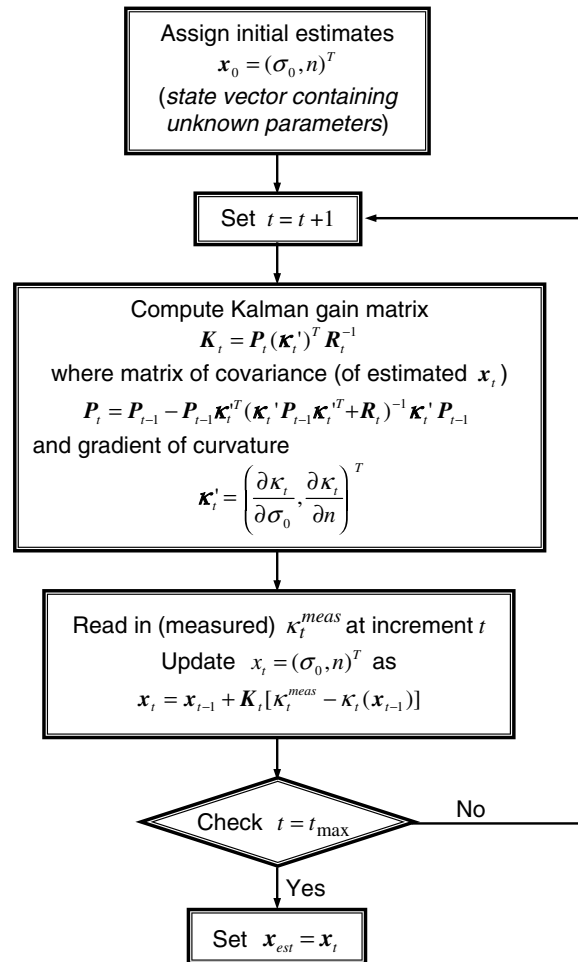
```
┌─────────────────────────────┐
│   Assign initial estimates   │
│   x₀ = (σ₀, n)ᵀ              │
│   (state vector containing   │
│   unknown parameters)        │
└─────────────────────────────┘
            │
            ▼
┌─────────────────────────────┐
│       Set  t = t +1          │◄──────────┐
└─────────────────────────────┘           │
            │                              │
            ▼                              │
┌───────────────────────────────────────┐ │
│   Compute Kalman gain matrix           │ │
│   Kₜ = Pₜ(κₜ')ᵀ Rₜ⁻¹                    │ │
│ where matrix of covariance             │ │
│ (of estimated xₜ)                      │ │
│ Pₜ = Pₜ₋₁ − Pₜ₋₁κₜ'ᵀ(κₜ'Pₜ₋₁κₜ'ᵀ+Rₜ)⁻¹κₜ'Pₜ₋₁ │
│ and gradient of curvature              │ │
│ κₜ' = (∂κₜ/∂σ₀, ∂κₜ/∂n)ᵀ               │ │
└───────────────────────────────────────┘ │
            │                              │
            ▼                              │
┌───────────────────────────────────────┐ │
│ Read in (measured) κₜᵐᵉᵃˢ at increment t │ │
│ Update xₜ = (σ₀, n)ᵀ as                │ │
│ xₜ = xₜ₋₁ + Kₜ[κₜᵐᵉᵃˢ − κₜ(xₜ₋₁)]      │ │
└───────────────────────────────────────┘ │
            │                              │
            ▼                         No   │
        ◇ Check t = t_max ◇ ──────────────┘
            │ Yes
            ▼
┌─────────────────────────────┐
│    Set  x_est = xₜ           │
└─────────────────────────────┘
```

The Kalman filter procedure equations as shown:

$$\boldsymbol{x}_0 = (\sigma_0, n)^T$$

Compute Kalman gain matrix

$$\boldsymbol{K}_t = \boldsymbol{P}_t(\boldsymbol{\kappa}_t')^T \boldsymbol{R}_t^{-1}$$

where matrix of covariance (of estimated $\boldsymbol{x}_t$)

$$\boldsymbol{P}_t = \boldsymbol{P}_{t-1} - \boldsymbol{P}_{t-1}\boldsymbol{\kappa}_t'^T(\boldsymbol{\kappa}_t'\boldsymbol{P}_{t-1}\boldsymbol{\kappa}_t'^T + \boldsymbol{R}_t)^{-1}\boldsymbol{\kappa}_t'\boldsymbol{P}_{t-1}$$

and gradient of curvature

$$\boldsymbol{\kappa}_t' = \left(\frac{\partial \kappa_t}{\partial \sigma_0}, \frac{\partial \kappa_t}{\partial n}\right)^T$$

Read in (measured) κ_t^{meas} at increment t. Update $\boldsymbol{x}_t = (\sigma_0, n)^T$ as

$$\boldsymbol{x}_t = \boldsymbol{x}_{t-1} + \boldsymbol{K}_t[\kappa_t^{meas} - \kappa_t(\boldsymbol{x}_{t-1})]$$

Check $t = t_{max}$

Set $\boldsymbol{x}_{est} = \boldsymbol{x}_t$

Fig. 6. Flowchart of Kalman filter procedure to estimate the unknown parameters.

5. Verification study

Prior to implementing the proposed procedure to estimate unknown properties of TS ceramic coatings, the inverse analysis was carried out with simulated measurements from input parameters. Since correct solutions are known in such a study, it can be used to evaluate the accuracy and robustness of the present procedure.

5.1. Geometrical model

Several different types of models were constructed to evaluate the suitability and accuracy of the proposed procedure to extract the unknown material parameters. They are

1. nonlinear bi-material model based on the beam theory (from (10));
2. finite element model with complete substrate and coating from beginning (no re-meshing);
3. finite element model with element layer-by-layer build-up of coating (only vertically);
4. finite element model with elements build-up along both horizontal and vertical directions.

In all models, curvature–temperature relations were generated with inputs of fictitious material parameter values. These relations were then used to estimate or back-track the material parameters. In Model 1, since

the same equations are used to generate and extract the parameters, the inverse analysis was able to estimate essentially the same values as the input parameters. In Model 2, a finite element model of Al substrate and YSZ coating was constructed and the temperature was raised to generate the curvature with the CTE mismatch. As in Model 1 case, there was no residual stress at the room temperature which coincided with the zero-curvature temperature. For defining the stress–strain of coating, the constitutive relation (2) with arbitrary values were assigned for E_c, σ_0 and n. Again the proposed procedure was able to estimate the parameters accurately.

Unlike the first two models, more complex approaches were taken in Models 3 and 4. Here, actual deposition processes of YSZ coating were closely replicated in the finite element analyses. Essentially the spraying process was imitated by adding new stress-free elements on previously deposited elements. This characterizes a continuous deposition process of coating. Similar works were carried out by Bengtsson and Persson (1997) and Lugscheider and Nickel (2003). The difference between Models 3 and 4 is that a layer of elements which covers the *entire specimen length* is added each time in Model 3 while the process was much more refined in Model 4. The detail of Model 3 is not given here due to space limitation but the procedure of Model 4 is described next.

In the actual TS process, a plasma gun is moved transversely to deposit molten particles. The number of spray passage depends on required thickness of coating. From a sample fabrication, it is set at 15 passages with the final thickness of coating at $t = 277$ μm here. The substrate has the thickness of $h = 3.2$ mm. The re-meshing process during the element build-up is illustrated in Fig. 7. At each pass, the coating deposition (18.5 μm build-up) is simulated by adding five layers of elements. Since the spray deposition rate varies with the radial distance (more near the center of spray), the element additions were carried out as a moving inclined slope as depicted. The sizes of elements were chosen carefully to optimize the accuracy and computational time. In total 4500 elements were used for the coating and 2400 elements for the substrate. A significant amount of computational time was required to carry out this simulation since the re-meshing was carried out 960 times. Here, the specimen length is set at 40 mm, which is shorter than actual specimens but large enough compared to the thicknesses.

5.2. Thermal and heat flow conditions

A special care was also taken for the thermal and heat flow conditions to replicate the actual spray process as close as possible. During the deposition and cooling down periods, the heat is continuously taken away by forced air convection while deposited molten particles heat up the specimen. The heat flux out of surfaces was modeled with the following equation:

$$q_{\text{out}} = \tilde{h}(T - T_\infty) \tag{16}$$

Here, $\tilde{h}$ is heat transfer coefficient, T_∞ is ambient temperature and T is the surface temperature. To determine the suitable values of $\tilde{h}$ and the heat input q_{in}, a separate inverse analysis was performed. Although details cannot described here due to space limitation, transient heat transfer analyses and the Kalman filter were utilized to fit the measured temperature record with the simulated temperature. From this analysis, the coefficient is chosen as $\tilde{h} = 45$ W/m² K. If specimens are fabricated under similar conditions (e.g., same location), this parameter should be nearly constant for all cases. However the heat input through the molten particles changes depending upon each TS deposition process. For the simulated results given here (although not shown, several were carried out), the input flux is set to be $q_{\text{in}} = 210$ W/m². In addition, the temperature of newly deposited particle is set as $T = 330$ °C to match the measured results. Although molten particles have much higher temperature, as soon as they strike the substrate, the temperature drops immediately. Note their solidification process was not modeled here. Once the deposition is completed, the specimen was cooled down through the top and bottom surfaces according to (16). These heat flow conditions are illustrated in Fig. 7.

5.3. Materials

In the tests, Al6061 plates were used for the substrates. Since it is sensitive to temperature change, its properties were modeled as temperature dependent. The Young's modulus and the coefficient of thermal expansion follow (Material Properties Database, 1999)
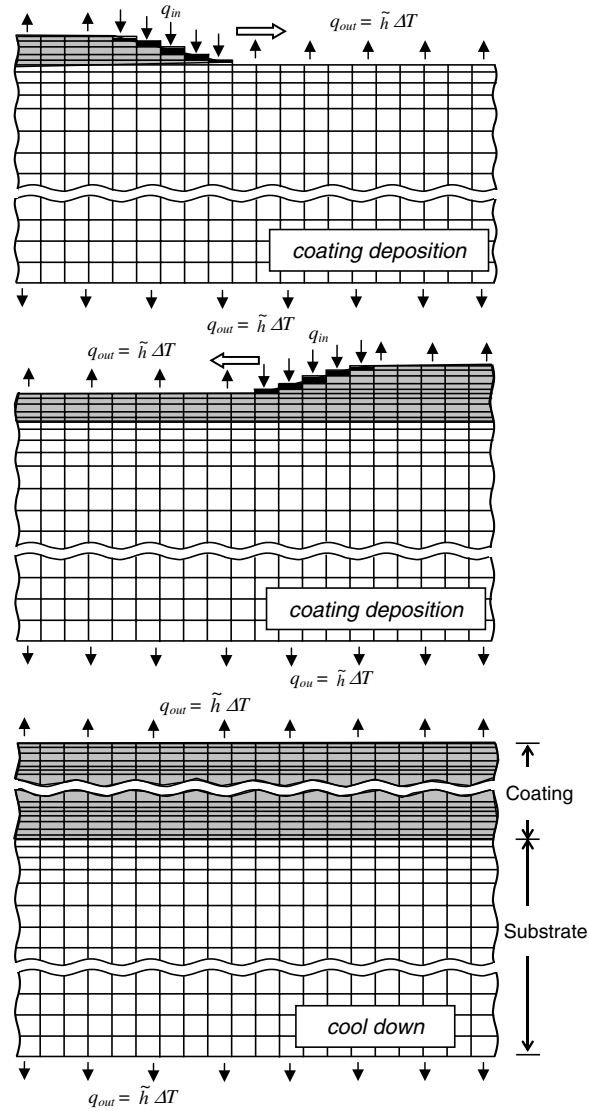
Fig. 7. Accurate simulation of TS deposition process through adding elements along transverse direction under proper heat transfer. The bottom figure shows cool down of completed deposition.

$$E_s(T) = -2.65 \times 10^{-7}T^3 + 2.4 \times 10^{-4}T^2 - 9.21 \times 10^{-2}T + 85.2 \ (\text{GPa}) \quad \text{for } 113 \ \text{K} < T \leqslant 573 \ \text{K}$$
$$\alpha_s(T) = -9.27 \times 10^{-12}T^2 + 2.59 \times 10^{-8}T + 1.54 \times 10^{-5} \ (1/\text{K}) \quad \text{for } 283 \ \text{K} < T \leqslant 575 \ \text{K} \tag{17}$$

Only the temperature ranges relevant to the present tests are noted above. Although the temperature reaches only up to ∼250 °C (523 K) during thermal cycle tests, the inclusion of temperature dependent properties is very important in the estimations. Without them, the coating property would be estimated less nonlinear than the actual.

Since the stress does not reach very high during thermal cycle, plastic flow in the aluminum substrate was not considered. However yielding probably occurs when it is struck with molten particles during fabrication. The other parameters for the aluminum were chosen as $v_{Al} = 0.33$, mass density $\rho_{Al} = 2702 \ \text{kg/m}^3$, thermal conductivity $K_{Al} = 155 \ \text{W/m K}$ and specific heat capacity $c_{Al} = 963 \ \text{J/kg K}$. For the coating, the mechanical property was assumed to follow the nonlinear relation shown in (3). In the simulation shown here, the parameters were chosen as $E_c = 22.8 \ \text{GPa}$, $v = 0.32$, $\sigma_0 = 38 \ \text{MPa}$, $n = 2.65$, $\sigma_T = -22.1 \ \text{MPa}$ at $T_T = 30 \ °\text{C}$. Other

parameters include $\rho_{YSZ} = 5436$ kg/m^3, $K_{YSZ} = 1.0$ W/m K and $c_{YSZ} = 360$ J/kg K. These are representative values of TS YSZ coatings.

5.4. Simulated curvature–temperature measurements

The finite element analysis was carried out under transient coupled heat-transfer and stress condition. The computed temperature and curvature are shown as function of time in Fig. 8. Here, the temperature is obtained at the mid-point on the bottom surface where a thermocouple is attached in the actual tests. Also as in the experiments, the substrate is pre-heated to 160 °C. To report the curvature, it was computed from deflections at three points (consistent with experiments) as shown in Fig. 1.

In Fig. 8, the oscillatory behavior during deposition in both temperature and curvature experimental measurements signifies the spray passages. This phenomenon was accurately captured in the computational simulations. The oscillations are caused by passing of spray gun in the experiment and traverse additions of elements in the simulation. The noise or higher frequency oscillations observed in the experiment are due to high velocity particles striking onto to the substrate, which is not simulated in the finite element analysis. After 4–5 spray passes, the substrate temperature appears to reach the steady state. This suggests the heat input from particles and the heat removed from the specimen are approximately equilibrated. Since new elements added to the substrate have high temperature and they immediately cool down, the state of stress in the coating is tensile. These stresses cause the curvature to increase during the deposition as shown in Fig. 8(b). After the deposition is completed at $t = 190$ sec, both substrate and coating immediately cools down (from
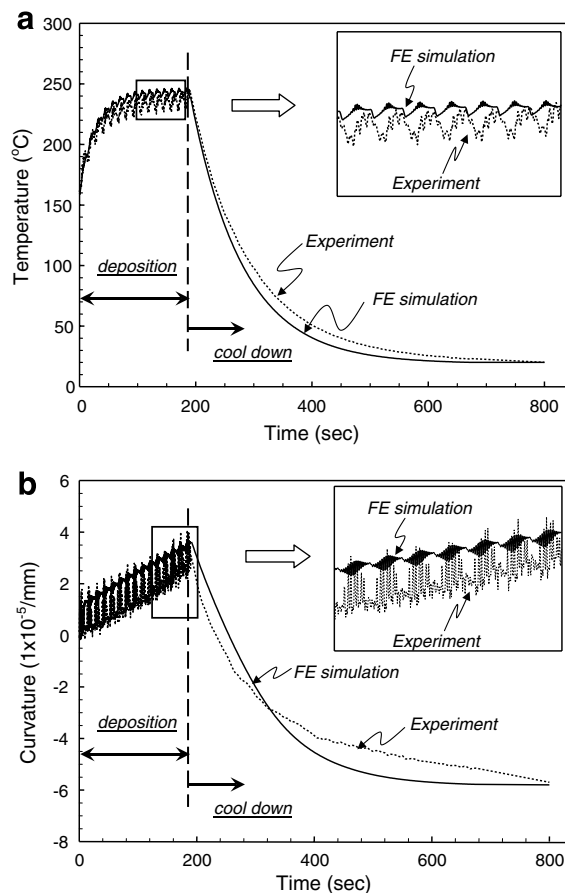
Fig. 8. Simulated (a) temperature and (b) curvature results from simulation. For comparison experimental results are also shown. Magnified curves in insets have different coordinate scales.

246 °C to 20 °C). During the cool down phase, the same heat transfer coefficient $\tilde{h} = 45 \text{ W/m}^2 \text{ K}$ in (16) was imposed across the substrate and coating surfaces. Since the CTE of substrate is higher than that of coating, the curvature reverses its sign and it eventually makes the overall stress in the coating to be compressive. Note, although the initial temperature of elements was adjusted to match with the measurements during the deposition, these temperature and curvature results during cool-down were not imposed at the respective measured locations.

From the curvature and temperature results during the cool down, the curvature temperature relation is obtained as shown in Fig. 9(a). This relation is used to back-track the material parameters as described in the next section. In Fig. 9(b), the through-thickness axial stresses are shown at four different temperatures. High stress gradients are observed in both Al substrate and YSZ coating in the boundary layer across the interface. These so-called quenching stresses were generated since the difference between particle and substrate temperatures during the first deposition pass is very high. Furthermore, unlike in the substrate, the stress variation is not linear even outside this boundary layer in the coating. It is nearly constant in the top half of coating. The average stresses in the coating are 9.7 MPa, −2.4 MPa, −23.7 MPa and −27.3 MPa at the maximum, zero-curvature, transition and room temperatures, respectively. It is interesting to observe that at the zero-curvature, the average stress is not zero due to the nonlinear through-thickness variation of stress. We also note that in real specimens, the stress states are more inhomogeneous due to high local solidification stresses in particles. In fact, these high tensile stresses are the causes of many intra-splat cracks (Teixeira et al., 1999). The magnitude of residual stress at the room temperature is also relevant in terms of defining the stress–strain relation. The compressive stress keeps micro-cracks from extending. However, under high temperature
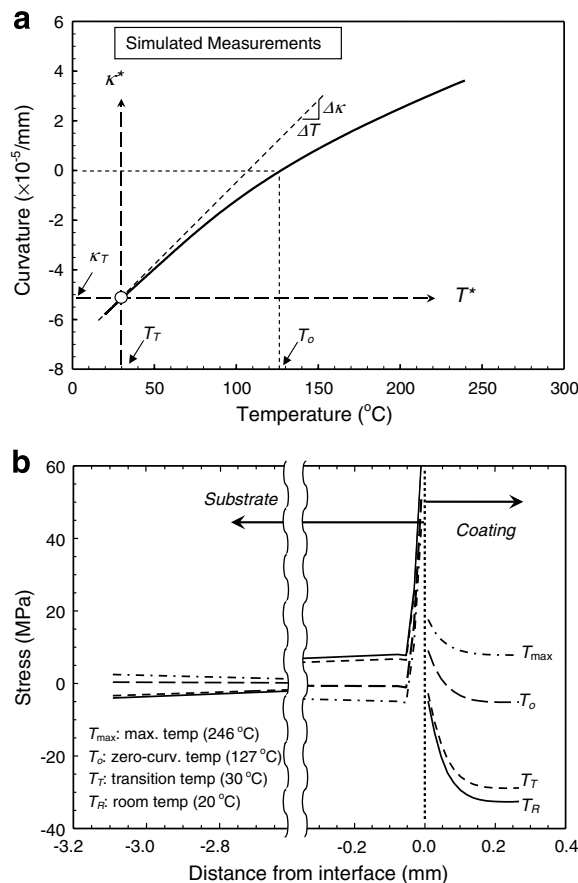

Fig. 9. (a) Simulated curvature–temperature record during cool-down. Key curvature and temperatures are noted. (b) Axial stress through thickness at different temperatures.

environments, the stresses with in coatings generally return to tensile states. It is reminded that these stresses *vary* according to processing conditions, including coating thickness, pre-heat temperature and others. Alternatively, one may generate a desired stress state with suitable processing conditions.

5.5. Estimated material parameters

From the simulated curvature–temperature relation shown in Fig. 9(a), the proposed procedure was carried out to extract the material parameters. First, the transition curvature and temperature were identified as $\kappa_T = -5.2 \times 10^{-5}$/mm and $T_T = 30\,°C$, respectively. Since the curvature change is gradual, precise determination of the transitional point is difficult. However, our analysis (to be shown later) demonstrates the precise determination of T_T is not so critical in re-construction of the stress–strain relation. Using the linear slope between $T = 20\,°C$ and $30\,°C$ and the curvature formula (1), the Young's modulus of the coating is estimated as $E_c = 23.2\,GPa$, which is 1.8% off from the imposed modulus (22.8GPa).

Next, parameters σ_0 and n were estimated with the Kalman filter procedure described in Section 4 after adjusting the curvature–temperature relation to T^*–κ^* coordinates as shown in Fig. 9(a). Here, we have selected 25 curvatures and temperatures at time increment of $dt = 10\,s$ for $t > 200\,s$ for the inputs in the Kalman filter. The initial estimates of σ_0 and n were chosen as follows. Within the ranges of $10\,MPa < \sigma_0 < 90\,MPa$ and $1 < n < 4$, σ_0 and n were incremented into forty separate values to generate $41 \times 41 = 1681$ sets of initial estimates. Each set of initial estimates is processed through the Kalman filter and the final estimates are obtained after 25 steps. In general, different initial estimates do not merge at the same point but a robust procedure should generate a *small domain of convergence*. The *intensity of converge plot* is created from the 1681 sets of final estimates as shown in Fig. 10. Here, high intensity regions imply greater convergence of initial estimates. The best estimates can then be made from either the location where the highest intensity occurs or the weighted average as marked in the figure. They are $\sigma_0 = 35.6\,MPa$ and $n = 2.53$, respectively (input values: $\sigma_0 = 38\,MPa$, $n = 2.65$).

Finally, the remaining material parameter, the transitional stress was computed as $\sigma_T = -21.2\,MPa$ (~4% lower than the input). The residual stress at room temperature is also calculated as $\sigma_R = -24.5\,MPa$, which is ~10% different from the average residual stress through-thickness shown in Fig. 9(b). Using these estimated parameters, the stress–strain relation was re-constructed according to (3) as shown in Fig. 11. Here, the prescribed or input/exact stress–strain relation is also shown with the circles. Although each estimated parameter is slightly off from the corresponding input value, the agreement between two stress–strain curves is surprising. In fact, the two results essentially overlaps with each other.
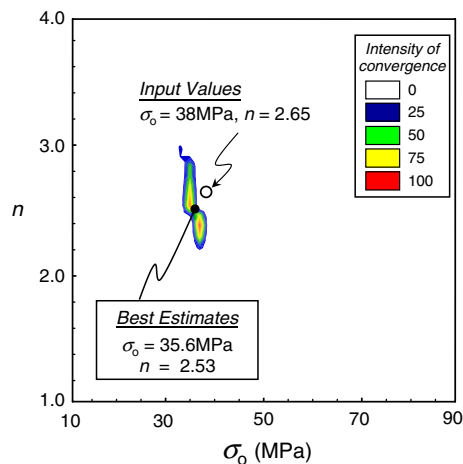

Fig. 10. Intensity of convergence plot generated from the inverse analysis from simulated TS deposition and cool down. A high intensity represents convergence of many initial estimates and likely location of best estimates. The scale of intensity (i.e., 0–100) is relative. The location of input values is also noted.
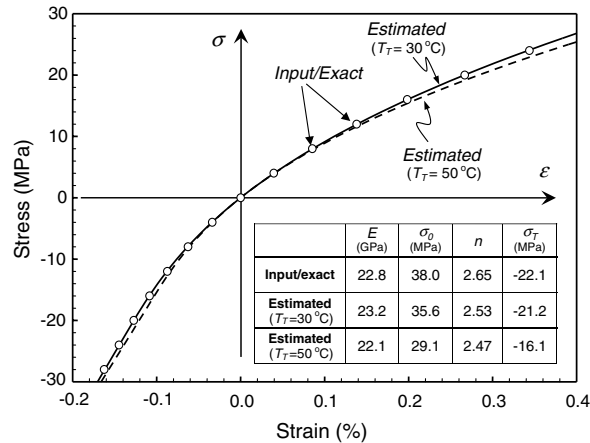
Fig. 11. Re-constructed stress–strain relations based on estimated (solid line) and input/exact (circles) parameters. Note estimated result ($T_T = 30\,°C$) nearly overlaps with the input/exact relation. Estimated result with a different transitional temperature ($T_T = 50\,°C$) is also shown for comparison.

As noted earlier, one possible difficulty in this procedure is identification of the transitional temperature. Suppose $T_T = 50\,°C$ was chosen instead of $T_T = 30\,°C$. With this T_T, the inverse analysis was re-carried out and the unknown parameters were estimated according to the same inverse procedure. The resulting stress–strain curve is shown in Fig. 11. There are clearly larger errors than those estimated with $T_T = 30\,°C$. However, the stress–strain curve of $T_T = 50\,°C$ is still close to the input/exact curve. Thus some deviation of T_T does not alter the overall stress–strain relation. These results should support the effectiveness of present procedure.

6. Nonlinear properties of TS YSZ coatings

After successful verification study, the procedure was utilized with the experimentally measured curvature–temperature data described in Section 2.2 and shown in Fig. 1(b). Here, TS YSZ coating was deposited onto aluminum plate and the specimen was thermal cycled several times subsequently. The behavior of specimen during the thermal cycles was repeatable and exhibited essentially the same substrate–curvature records.

As in the case of verification analysis, the temperature-curvature record was first used to identify the transitional temperature. Here, it was identified as $T_T = 30\,°C$ as illustrated in Fig. 5. The corresponding transitional curvature is $\kappa_T = -6.8 \times 10^{-5}$/mm. Then using the nearly linear slope $\Delta\kappa/\Delta T$ between $T = 20\,°C$ and $30\,°C$, the initial tangent modulus was estimated as $E_c = 22.4$ GPa with (1).

Next, the two parameters σ_0 and n were estimated with the Kalman filter procedure with the adjusted curvature–temperature relation on T^*–κ^* coordinates as shown in Fig. 5. Here, we have selected 25 curvatures within $30\,°C < T^* < 207\,°C$ for the inputs in the Kalman filter. Then, the approach described in the verification analysis was followed to constructed the *intensity of converge plot* shown in Fig. 12. The best estimates were determined as $\sigma_0 = 31.8$ MPa and $n = 2.15$, respectively. Te transitional stress and the residual stress were also obtained as $\sigma_T = -16.7$ MPa and $\sigma_R = -18.1$ MPa, respectively.

Using these parameters, the estimated stress–strain relation is shown in Fig. 13(a). The two shaded circles represent the stresses at the room temperature (20 °C) and the maximum temperature (207 °C). Essentially, the slopes outside these points represent *extrapolated* results since only the records between these temperatures were actually used to identify the unknown parameters. These bounds are important since the actual coatings may act differently outside the range, especially under large tensile stress (e.g., cracking).

In most inverse analyses, there is no independent way to prove that best estimates are indeed correct or near-correct solutions. However, there are two ways to judge their accuracy. One is from the sizes of converged regions shown in the intensity of convergence plot. A small region implies the robustness of inverse method as many initial estimates converged near the same location (i.e., similar estimates). The converged region shown in Fig. 12 is well contained and supports the accuracy of the estimates. An additional
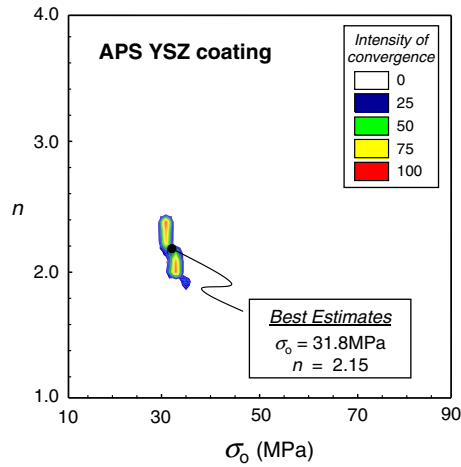
Fig. 12. Intensity of convergence plot generated by the inverse analysis from measured curvature–temperature. The location of best estimates is determined from weighted averages of convergence.
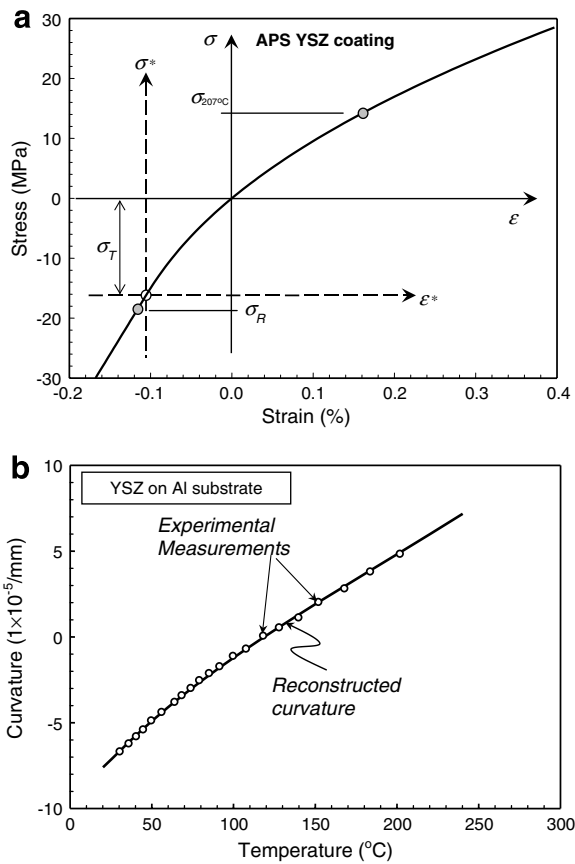

Fig. 13. (a) Nonlinear constitutive relation of TS YSZ coating estimated by the inverse analysis. (b) Comparison between measured and simulated results obtained by assigning the best estimates as input properties in the nonlinear bi-material formula.

confirmation can be made from re-creation of curvature–temperature relation. Using the best estimates as input parameters, the curvature–temperature relation was computed using the nonlinear bi-material solution

as shown in Fig. 13(b). The agreement with the measured curvature is excellent as the re-constructed curve fits within the bound of measurements.

Although not shown here, many other TS YSZ coatings as well as alumina coatings were tested with the proposed procedure. Most specimens demonstrated good convergence characteristics although some (∼10%) did not show good results. Though, it is yet to be confirmed in all cases, partial decohesion between the coating and substrate was observed in those specimens. This should be one of causes for failed convergences.

7. Discussion

In the present study, a novel method to estimate the nonlinear elastic properties of TS ceramic coating is proposed and examined closely. The unique nonlinear behavior of TS coatings is driven by their morphology (e.g., crack opening/closing). Our main goal was to establish a method which requires minimal specimen preparation as well as testing effort. Since each TS coating may possess different morphology and stress–strain relation, a simple and versatile test is valuable in conducting tests on various coatings. In this approach, measured curvature–temperature records are post-processed by the inverse analysis, namely the Kalman filter method. Furthermore, to circumvent large computational efforts, a nonlinear bi-material beam solution was derived. Although it still requires iterative calculations, the solution enables the data processing to be carried out without complex computational tools such as a finite element method.

Our verification analysis proved the high accuracy as well as the robustness of the proposed procedure. In fact, the extracted stress–strain relation was very close to the one prescribed in the model. The proposed procedure was also implemented to estimated the nonlinear stress–strain relation of actual TS YSZ coating on aluminum substrate. The small converged area of various estimates as well as the good match with the measured curvature suggested the high degree of accuracy in the estimated parameters. The present method can be extended to determine nonlinear material properties of other films and coatings using the substrate curvature measurements.

In addition, a detailed finite element procedure was introduced to replicate the deposition process of thermally sprayed coatings accurately in the verification study. The geometrical change as well as the thermal heat flux conditions are modeled in this simulation. This model also offers good insights into the internal stress states of coatings during the fabrication and cool down periods. Although not within the scope of this study, a similar procedure can be used to evaluate various effects of processing parameters on TS coatings. They include speed of deposition, substrate pre-heating, and coating thickness.

Acknowledgements

Appendix

Determination of average secant modulus through-thickness

In terms of σ^* and ε^* in (2), the average modulus is expressed as

$$E_{ave}^* = \frac{\sigma^*}{\varepsilon^*} = \begin{cases} E_c, & \sigma^* < 0 \\ \frac{E_c \sigma_0^{n-1}}{\sigma_0^{n-1} + (\sigma^*)^{n-1}}, & \sigma^* > 0 \end{cases} \tag{A.1}$$

Suppose ε, E_c, σ_0, and n are known, Newton's method can be used to determine σ^* for a given ε^* under $\sigma^* > 0$. First an implicit function is defined as

$$f(\sigma^*) = \frac{\sigma^*}{E_c} + \frac{(\sigma^*)^n}{E_c \sigma_0^{n-1}} - \varepsilon^* = 0 \tag{A.2}$$

Then the following iteration is carried out to determine σ^*:

$$\sigma_i^* = \sigma_{i-1}^* - \frac{f(\sigma_{i-1}^*)}{f'(\sigma_{i-1}^*)}, \quad \text{where } f'(\sigma_{i-1}^*) = \frac{1}{E_c}\left[1 + n\left(\frac{\sigma_{i-1}^*}{\sigma_0}\right)^{n-1}\right] \tag{A.3}$$

The convergence is satisfied when $|\sigma_i^* - \sigma_{i-1}^*| < 1 \times 10^{-3}\sigma_0/E_c$. Then (A.1) is used to compute E_{ave}^*.

Determination of transitional and residual stresses

To compute the transitional stress σ_T, first the average secant modulus E_{ave}^T between the zero-curvature and the transition point is computed in the following linear bi-material equation:

$$\frac{6E_s E_{\text{ave}}^T ht(h+t)\Delta\alpha(T_0 - T_T)}{E_s^2 h^4 + E_{\text{ave}}^{T2} t^4 + 2E_s E_{\text{ave}}^T ht(2h^2 + 3ht + 2t^2)} - (\kappa_0 - \kappa_T) = 0 \tag{A.4}$$

Then the following equation is used to solve for the transitional stress σ_T:

$$\sigma_T = \sigma_0\left(\frac{E_c}{E_{\text{ave}}^T} - 1\right)^{\frac{1}{n-1}} \tag{A.5}$$

To determine the residual stress at room temperature at the mid-point of coating σ_R, the following equation may be used:

$$\sigma_R = E_c(\kappa_R - \kappa_T)\left(h + \frac{t}{2} - y_0\right) + \frac{E_c E_s h}{E_s h + E_c t}\Delta\alpha(T_R - T_T) + \sigma_T \tag{A.6}$$

Here, T_R and κ_R are the room temperature and the corresponding curvature.

Determination of curvature gradients

Curvature κ^* changes as a function of σ_0 and n for given T, expressed as

$$\kappa^* = \frac{6E_s E_{\text{ave}}^* ht(h+t)\Delta\alpha T^*}{E_s^2 h^4 + (E_{\text{ave}}^*)^2 t^4 + 2E_s E_{\text{ave}}^* ht(2h^2 + 3ht + 2t^2)} \tag{A.7}$$

Here, $T^* = T - T_T$ and $\kappa^* = \kappa - \kappa_T$. Then the derivatives of κ^* with respect to σ_0 and n are

$$\frac{\partial\kappa^*}{\partial\sigma_0} = \frac{\partial\kappa^*}{\partial E_{\text{ave}}^*}\frac{\partial E_{\text{ave}}^*}{\partial\sigma_0} \quad \text{and} \quad \frac{\partial\kappa^*}{\partial n} = \frac{\partial\kappa^*}{\partial E_{\text{ave}}^*}\frac{\partial E_{\text{ave}}^*}{\partial n} \tag{A.8}$$

From (A.1), each partial derivative is expressed as

$$\frac{\partial\kappa^*}{\partial E_{\text{ave}}^*} = \frac{6E_s ht(h+t)(E_s^2 h^4 - (E_{\text{ave}}^*)^2 t^4)\Delta\alpha T^*}{(E_s^2 h^4 + (E_{\text{ave}}^*)^2 t^4 + 2E_s(E_{\text{ave}}^*)ht(2h^2 + 3ht + 2t^2))^2} \tag{A.9}$$

Also,

$$\frac{\partial E_{\text{ave}}^*}{\partial\sigma_0} = \frac{E_c(n-1)(\sigma^*)^{n-1}(\sigma_0^{n-1} + (\sigma^*)^{n-1})}{(\sigma_0^n + \sigma_0(\sigma^*)^{n-1})(\sigma_0^{n-1} + n(\sigma^*)^{n-1})} \quad \text{and} \quad \frac{\partial E_{\text{ave}}^*}{\partial n} = \frac{-E_c \ln(\sigma^*/\sigma_0)(\sigma^*)^{n-2}(\sigma_0^n \sigma^* + \sigma_0(\sigma^*)^n)}{(\sigma_0^n + \sigma_0(\sigma^*)^{n-1})(\sigma_0^{n-1} + n(\sigma^*)^{n-1})} \tag{A.10}$$

The above expressions are used in the Kalman filter algorithm.

References

Bengtsson, P., Persson, C., 1997. Modelled and measured residual stresses in plasma sprayed thermal barrier coatings. Surface and Coatings Technology 92, 78–86.

Carlotti, G., Doucet, L., Dupeux, M., 1997. Elastic properties of silicon dioxide films deposited by chemical vapour deposition from tetraethylorthosilicate. Thin Solid Films 296, 102–105.

Finot, M., Suresh, S., 1996. Small and large deformation of thick and thin film multi-layers: effects of layer geometry, plasticity and compositional gradients. Journal of Mechanics and Physics of Solids 44, 683–721.

Gu, Y., Nakamura, T., Prchlik, L., Sampath, S., Wallace, J., 2003. Micro-indentation and inverse analysis to characterize elastic–plastic graded materials. Materials Science and Engineering A 345, 223–233.

Harok, V., Neufuss, K., 2001. Elastic and inelastic effects in compression in plasma-sprayed ceramic coatings. Journal of Thermal Spray Technology 10 (1), 126–132.

Hunsche, B., Vergöhl, M., Neuhäuser, H., Klose, F., Szyszka, B., Matthée, T., 2001. Effect of deposition parameters on optical and mechanical properties of MF- and DC-sputtered Nb_2O_5 films. Thin Solid Films 392 (2), 184–190.

Kalman, R.E., 1960. A new approach to linear filtering and prediction problems. ASME Journal of Basic Engineering D 82, 35–45.

Kesler, O., Matejicek, J., Sampath, S., Suresh, S., Gnaeupel-Herold, T., Brand, P.C., Prask, H.J., 1998. Measurement of residual stress in plasma-sprayed metallic, ceramic and composite coatings. Materials Science and Engineering A 257, 215–224.

Kroupa, F., Dubsky, J., 1999. Pressure dependence of Young's moduli of thermal sprayed materials. Scripta Materialia 40 (11), 1249–1254.

Kroupa, F., Plesek, J., 2002. Nonlinear elastic behavior in compression of thermally sprayed materials. Materials Science and Engineering A 328, 1–7.

Krulevitch, P., Ramsey, P.B., Makowiecki, D.M., Lee, A.P., Northrup, M.A., Johnson, G.C., 1996. Mixed-sputter deposition of Ni–Ti–Cu shape memory films. Thin Solid Films 274, 101–105.

Kuroda, S., Fukushima, T., Kitahara, S., 1988. Simultaneous measurement of coating thickness and deposition stress during thermal spraying. Thin Solid Films 164, 157–163.

Kuroda, S., Fukushima, T., Kitahara, S., 1990. Generation mechanisms of residual stresses in plasma-sprayed coatings. Vacuum 41, 1297–1299.

Lacquaniti, V., Monticone, E., Picotto, G.B., 1997. Structural and surface properties of sputtered Nb films for multilayer devices. Surface Science 377–379, 1042–1045.

Lugscheider, E., Nickel, R., 2003. Finite element simulation of a coating formation on a turbine blade during plasma spraying. Surface and Coatings Technology 174–175, 475–481.

Matejicek, J., Sampath, S., 2003. In situ measurement of residual stresses and elastic moduli in thermal sprayed coatings: Part 1: apparatus and analysis. Acta Materialia 51, 863–872.

Matejicek, J., Sampath, S., Gilmore, D., Neiser, R., 2003. In situ measurement of residual stresses and elastic moduli in thermal sprayed coatings: Part 2: processing effects on properties of Mo coatings. Acta Materialia 51, 873–885.

Material Properties Database, 1999. JAHM Software, Inc.

Menzel, S., Strehle, S., Wendrock, H., Wetzig, K., 2005. Effect of Ag-alloying addition on the stress–temperature behavior of electroplated copper thin films. Applied Surface Science 252, 211–214.

Oka, Y., Tao, M., Nishimura, Y., Azuma, K., Fujiwara, E., Yatsuzuka, M., 2003. Properties of thick DLC films prepared by plasma-based ion implantation and deposition using combined RF and H.V. pulses. Nuclear Instruments and Methods in Physics Research B 206, 700–703.

Stoney, G., 1909. The tension of metallic films deposited by electrolysis. Proc Roy Soc London A 82, 172–175.

Teixeira, V., Andritschky, M., Fischer, W., Buchkremer, H.P., Stover, D., 1999. Effects of deposition temperature and thermal cycling on residual stress state in zirconia-based thermal barrier coatings. Surface and Coatings Technology 120–121, 103–111.

Tsui, Y.C., Clyne, T.W., 1997. An analytical model for predicting residual stresses in progressively deposited coatings: Part 1: planar geometry. Thin Solid Films 306, 23–33.

Vaddadi, P., Nakamura, T., Singh, R., 2003. Inverse analysis for transient moisture diffusion through fiber-reinforced composites. Acta materialia 51, 177–193.

Waki, H., Ogura, K., Nishikawa, I., Ohmori, A., 2004. Monotonic and cyclic deformation behavior of plasma-sprayed coatings under uni-axial compressive loading. Materials Science and Engineering A 374, 129–136.

Wang, W., Li, C., Wang, Y., Yang, G., Sonoya, K., 2006. Tensile deformation behavior of plasma-sprayed Ni–45Cr coatings. Surface and Coatings Technology 201, 842–847.